

Shallow Cumulus Cloud Fields Are Optically Thicker When They Are More Clustered

Pouriya Alinaghi^{*1}, Martin Janssens^{1,2}, Goutam Choudhury³, Tom Goren³, A. Pier Siebesma^{1,4}, and Franziska Glassmeier¹

¹Delft University of Technology, Delft, The Netherlands

²Wageningen University & Research, The Netherlands

³Bar-Ilan University, Ramat Gan, Israel

⁴Royal Netherlands Meteorological Institute (KNMI), De Bilt, The Netherlands

Date: September 19, 2023

Note: In the final stages of preparing this manuscript, we became aware of independent, related work by Denby (2023) (<https://doi.org/10.48550/arXiv.2309.08567>).

*Correspondence: p.alinaghi@tudelft.nl

abstract

Shallow trade cumuli over subtropical oceans are a persistent source of uncertainty in climate projections. Mesoscale organization of trade cumulus clouds has been shown to influence their cloud radiative effect (CRE) through cloud cover. We investigate whether organization can explain CRE variability independently of cloud cover variability. By analyzing satellite observations and high-resolution simulations, we show that increased clustering leads to geometrically thicker clouds with larger domain-averaged liquid water paths, smaller cloud droplets, and consequently, larger cloud optical depths. The relationships between these variables are shaped by the mixture of deep cloud cores and shallower interstitial clouds or anvils that characterize cloud organization. Eliminating cloud cover effects, more clustered clouds reflect up to 20 W/m^2 more instantaneous shortwave radiation back to space.

1 Introduction

Marine shallow cumulus clouds, as the most prevalent cloud type (Johnson, Rickenbach, Rutledge, Ciesielski, & Schubert, 1999), play a vital role in the climate system by reflecting incoming solar radiation back to space (Bony, Dufresne, Le Treut, Morcrette, & Senior, 2004; Bony & Dufresne, 2005; Bony et al., 2015). The response of these clouds to changes in cloud-controlling factors remains as one of the largest sources of uncertainty of climate projections (Schneider et al., 2017; Nuijens & Siebesma, 2019; Sherwood et al., 2020), despite recent advances (e.g., Vogel et al., 2022).

Shallow cloud fields in the trades exhibit a diverse range of patterns, which have subjectively, and almost poetically, been classified as *Sugar*, *Gravel*, *Flowers* and *Fish* (Stevens et al., 2020). A comprehensive analysis by Janssens et al. (2021) shows that the quantification of such patterns needs at least two effective dimensions. Cloud fraction f_c as a bulk 1D measure and the organization index I_{org} , which quantifies the level of non-randomness in cloud spatial distribution within a cloud field (Weger, Lee, Zhu, & Welch, 1992; Tompkins & Semie, 2017) are an example of a suitable variable choice to represent these two dimensions. How relevant this mesoscale organization is for the low-cloud climate feedback remains an open question.

The shortwave (SW) and longwave (LW) radiative effect of clouds is sensitive to organization (Denby, 2020). The daily mean cloud radiative effect (CRE) varies by approximately 10 W/m^2 among subjectively classified cloud patterns, primarily due to differences in f_c , with a variability of 5 to 10 W/m^2 at a fixed f_c (Bony, Schulz, Vial, & Stevens, 2020). Contrary to the case of deep convective clouds (Tobin, Bony, & Roca, 2012), where outgoing LW radiation increases with clustering, Luebke, Ehrlich, Schäfer, Wolf, and Wendisch (2022) suggest a correlation between increased I_{org} values and *reduced* LW warming. No influence of clustering on SW cooling is observed in their study. For stratocumulus cloud decks, McCoy, McCoy, Wood, Zuidema, and Bender (2022) demonstrate that different morphologies, indicative of differences in the horizontal organization of the cloud decks, modulate the relationship between albedo and f_c .

We aim to investigate whether – independent of f_c variability – the horizontal organization of shallow cumulus cloud fields has an impact on their net CRE. To do so, we combine satellite data with a large ensemble of large-eddy simulations (section 2). After

removing the confounding effect of cloud fraction (section 3.1), we show that clustered cloud fields feature optically thicker clouds (section 3.2). This stems from clustered cloud fields containing more liquid-water path and smaller retrieved cloud droplets (section 3.2). Analyzing the simulations establishes that increased liquid-water path due to increased clustering primarily results from increased cloud geometric thickness (section 3.3). Section 4 concludes.

2 Description of the Data

Following previous studies (Stevens et al., 2020; Bony et al., 2020; Janssens et al., 2021), we focus on clouds over the tropical Atlantic Ocean to the east of Barbados (10° - 20° N, 48° - 58° W), which are representative for the trades (Medeiros & Nuijens, 2016). Our analysis covers December to May of 2002 to 2020. Our satellite dataset combines data from NASA’s Moderate Resolution Imaging Spectroradiometer (MODIS) aboard the Aqua satellite, with data from the Clouds and the Earth’s Radiant Energy System (CERES) instrument. We compute organization metrics from MODIS’ cloud masks. For each cloudy scene, we calculate two metrics - cloud fraction (f_c) and degree of organization (I_{org}). The preprocessing of MODIS’ cloud masks follows Janssens et al. (2021): Scenes with $> 20\%$ cirrus coverage are excluded, as are cloud fields with solar zenith angles $> 45^{\circ}$. In contrast to Janssens et al. (2021), we use the full $10^{\circ} \times 10^{\circ}$ domain. Following Schulz, Eastman, and Stevens (2021), we focus solely on shallow clouds by excluding scenes with cloud-top heights $z_t > 4$ km. After preprocessing, approximately 750 cloud fields remain for analysis. CERES provides hourly top-of-the-atmosphere SW and LW radiative fluxes for all-sky and clear-sky conditions, as well as cloud optical depth (τ_c), cloud albedo (A_c), cloud-top height (z_t), liquid water path (\mathcal{L}), and cloud-droplet effective radius (r_e). We select CERES data around 13:30 local time, which corresponds to the overpass time of the Aqua satellite. Shortwave cloud radiative effect (SWCRE) and longwave cloud radiative effect (LWCRE) are calculated as the difference between the all-sky and clear-sky radiative fluxes at the top of the atmosphere. For each cloud scene, we calculate domain-mean values of cloud properties provided by CERES.

We amend our satellite analysis with the *Cloud Botany* dataset (Jansson et al., 2023). This is a large ensemble (ca. 100 members) of high-resolution (100 m) large-eddy simulations (LES) of shallow cumulus clouds with a domain size of 150 km by 150 km. It was initialized with a variety of conditions derived from ERA5 reanalysis data (Hersbach et al., 2020) of trade cumuli that cover the climatological conditions of the area under consideration. We refer to the dataset paper, Jansson et al. (2023), for details. Our motivation for employing the *Botany* simulations is twofold. Firstly, considering that liquid-water path \mathcal{L} and effective radius r_e might be underestimated in less organized conditions of broken cloud fields containing small clouds (Zhang & Platnick, 2011; Seethala & Horváth, 2010; Painemal & Zuidema, 2011), the simulations support that our results are physical. Secondly, the simulations provide data on cloud-base height (z_b) and cloud geometric thickness (h) so that we can investigate how they are correlated to organization. We use hourly data from hours 37-43 of the simulations (574 cloud fields in total). These times are chosen because they approximately align with the daily overpass times of the Aqua satellite to match the diurnal phase. To determine the geometric thickness h of each cloudy column, we calculate the difference between the altitudes of the highest and lowest cloudy pixels where the liquid water specific humidity is larger than zero. Subsequently,

for each cloud field, we compute the domain-averaged h . We further compute the mean size of cloud objects within each cloud field using: $L_c = (\sum_1^n A_i)/n$, where A_i represents the area of each individual cloud object i , and n corresponds to the total number of cloud objects within the field.

3 Results & Discussions

3.1 Cloud organization impacts CRE independent of f_c variability

Figure 1(a-c) shows that as clouds become more organized (increasing I_{org}), they reflect less SW radiation towards space (smaller magnitude of SWCRE). In addition, increased organization also leads to a decrease in LWCRE. Overall, the warming effect induced by the SW component is partially compensated by the reduced LW warming. Consequently, enhanced organization of clouds results in diminished net cloud radiative cooling.

It is crucial to emphasize that the relationships illustrated in Fig. 1(a-c) are confounded by the variability of f_c , as f_c is correlated with I_{org} , SWCRE, and LWCRE (Fig. S1). To eliminate the confounding effect of f_c , we employ the concept of partial correlation analysis (Baba, Shibata, & Sibuya, 2004). For any given metric (e.g., X), we eliminate the variability associated with f_c using a regression analysis,

$$X = c \times f_c + X|f_c, \quad (1)$$

where f_c serves as the regressor, c represents the coefficient, and $X|f_c$ denotes the remaining variability in X that cannot be explained by f_c .

Fig. 1(d) shows that as $I_{org}|f_c$ increases, $SWCRE|f_c$ becomes more negative, i.e., as clouds cluster, they reflect more incoming SW radiation. The resulting SW cooling amounts to up to 20 W/m^2 . This indicates that the positive correlation observed in Fig. 1(a) is due to I_{org} and SWCRE being negatively correlated to f_c (Fig. S1, a, b). Similarly, after elimination of f_c variability, the response of LWCRE to cloud organization is strongly reduced to about 1 W/m^2 (Fig. 1, e), indicating that the correlation between I_{org} and LWCRE in Fig. 1(b) is almost solely due to their mutual correlation with f_c (Fig. S1, c). The variability in LWCRE due to clustering is thus similar in magnitude to the LW radiative effect ($\approx 0.75 \text{ W/m}^2$) of the “cloud twilight zone” (Eytan, Koren, Altaratz, Kostinski, & Ronen, 2020). Ultimately, as Fig. 1(f) illustrates, the dependence of net CRE on $I_{org}|f_c$ arises almost exclusively from the dependence of the SW component on cloud organization.

3.2 Clustering and cloud optical thickness are positively correlated

In the previous section, we eliminated the impact of f_c on the I_{org} -SWCRE relationship. The remaining variability in SWCRE is caused by variations in albedo and could be modulated by a sensitivity of 3D radiative effects to cloud organization. Regarding the latter, Singer, Lopez-Gomez, Zhang, and Schneider (2021) report that biases in top-of-the-atmosphere SWCRE from neglecting 3D radiative effect are negligible for both, unorganized and organized shallow cumulus cloud fields (their Fig. 7). This is especially expected for averages over large domains, as analyzed here. Indeed, a bi-linear regression

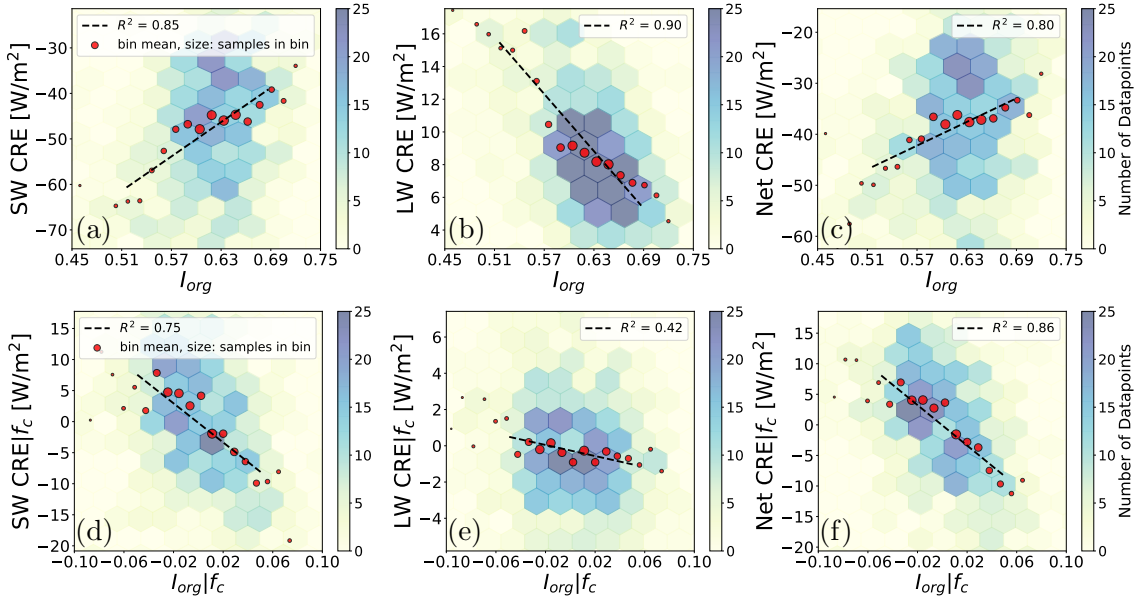


Figure 1: Dependence of domain-mean CRE on organization. In the first row (a-c), the relationships between I_{org} and SWCRE (a), LWCRE (b), and net CRE (c) are illustrated. The second row (d-f) shows the same relationships but with removing the f_c variability. The mean values of I_{org} (for the 2nd row, $I_{org}|f_c$) in each bin are denoted by red circles, with their size proportional to the number of points in the bin. The red dots are fitted with a dashed black line. Values below the 5th and above the 95th percentile of I_{org} (for the 2nd row, $I_{org}|f_c$) are excluded from the fit.

with f_c and albedo as regressors can explain 94 % of variability in SWCRE in our dataset (Fig. S2). This confirms that the impact of 3D radiative effects is negligible in these large cloud fields.

Having 3D effects excluded, the remaining variability in SWCRE primarily corresponds to changes in albedo and equivalently cloud optical depth τ_c . Figure 2(a) displays the variability of cloud patterns in a plane spanned by $\tau_c|f_c$ and $I_{org}|f_c$. This figure shows a continuous range of patterns, in the terminology of Stevens et al. (2020) ranging from *Sugar* and *Gravels* in the lower left corner to *Fish* and *Flowers* in the upper right corner.

On average, $\tau_c|f_c$ increases with increasing $I_{org}|f_c$ (Fig. 2, b). Despite the seemingly modest increase in $\tau_c|f_c$, such changes can result in a significant increase in albedo of 0.03 to 0.04 (Figs. S3, S4), and the notable increase in SW reflection by 20 W/m² (Fig. 1, d). The $I_{org}|f_c$ - $\tau_c|f_c$ relationship indicates that horizontal cloud field organization, as measured by I_{org} , directly corresponds to its vertical organization, as captured by τ_c : trade cumuli are optically thicker when they are more clustered.

As theoretically expected (Han, Rossow, & Lacis, 1994), τ_c is proportional to \mathcal{L}/r_e in our dataset (Fig. S5). Figure 3 shows that both, \mathcal{L} and r_e , contribute to mediating the relationship between organization and optical depth. With the f_c effect eliminated, there is a positive correlation between the degree of cloud clustering and the amount of liquid water present within the clouds (Fig. 3, a). Similarly, as the level of clustering increases, clouds tend to exhibit smaller radii r_e (Fig. 3, b). A cloud field that is dominated by *Flowers* shows smaller radii r_e but higher liquid-water path \mathcal{L} compared to the field dominated by *Sugar* and *Gravels*.

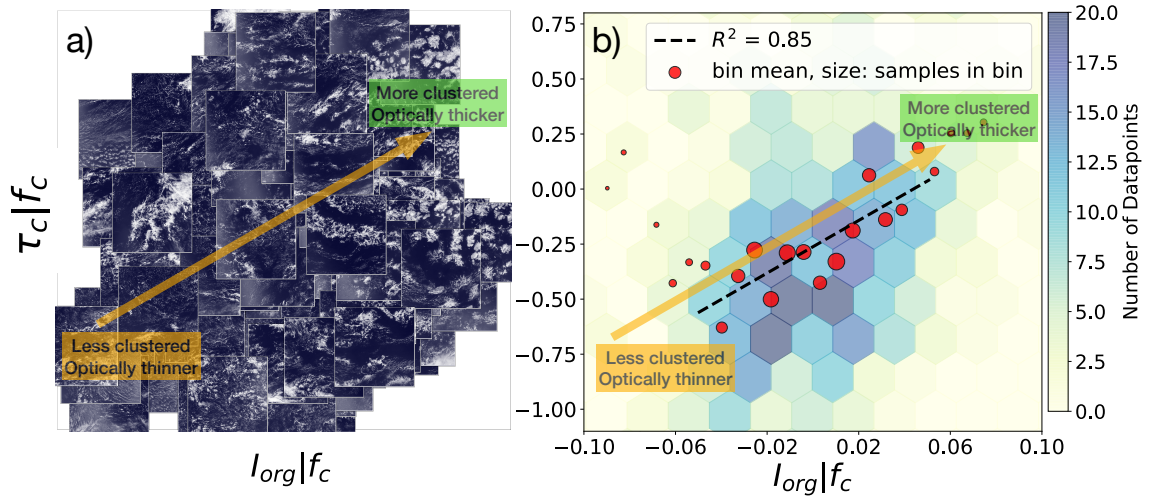


Figure 2: Dependence of domain-mean cloud optical depth on organization. The scatter plot of MODIS cloud features (a) and the 2-dimensional histogram (b) depict the $I_{org}|f_c - \tau_c|f_c$ relationship. Specifically, for the scatter plot in (a), instead of displaying individual points, the entire cloud field is visualized to enhance pattern visualization. Clouds are represented in white, while the blue background represents the ocean color (MODIS true-color images). For plot (b), the mean values of $I_{org}|f_c$ in each bin are denoted by red circles, with their size proportional to the number of points in the bin. The red dots are fitted with a dashed black line. Values below the 5th and above the 95th percentile of $I_{org}|f_c$ are excluded from the fit.

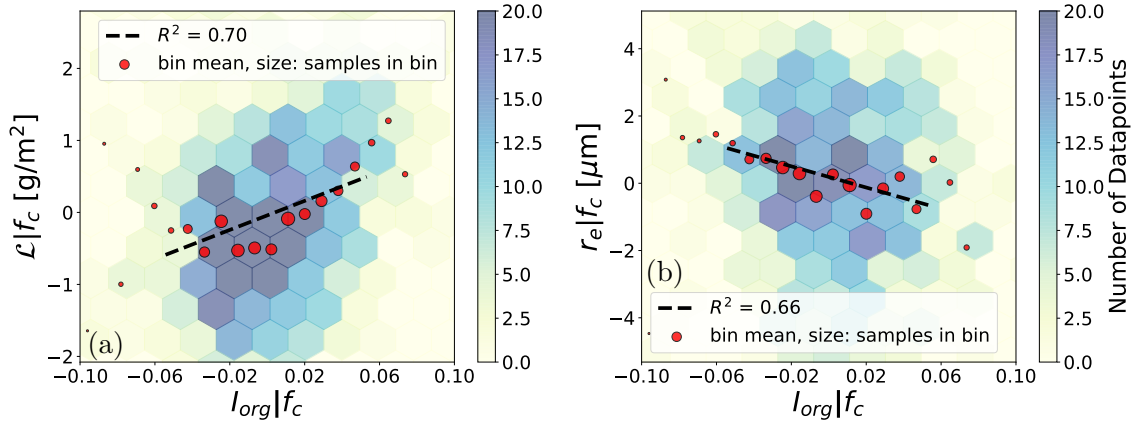


Figure 3: Dependence of domain-mean liquid water path and effective radius on organization. The figure shows the 2D histograms of the relationships between $I_{org}|f_c$ and $\mathcal{L}|f_c$ (a), and between $I_{org}|f_c$ and $r_e|f_c$ (b). The mean values of $I_{org}|f_c$ in each bin are denoted by red circles, with their size proportional to the number of points in the bin. The red dots are fitted with a dashed black line. Values below the 5th and above the 95th percentile of $I_{org}|f_c$ are excluded from the fit.

Our \mathcal{L} -organization relationship seems to be in contrast to Schulz et al. (2021) who show that individual *Gravel* clouds have higher liquid-water path \mathcal{L} compared to individual *Flowers*. To reconcile this with our results, we need to remind ourselves that the large cloud scenes analyzed here contain a mixture of different clouds. Stevens et al. (2020)

report that *Gravel* clouds tend to coexist with *Sugar*. For *Flowers* such a coexistence is less pronounced. Instead, *Flowers* feature anvils. Such shallow cumulus anvils have notable geometric thickness (200 m (Wood et al., 2018) to 600 m (Dauhut et al., 2023)). This means that anvil cloudiness is optically thicker and more reflective than typical *Sugar* (see also Fig. 7 in Stevens et al. (2020)). When considering two cloud fields with identical f_c , it therefore seems reasonable that a *Flower*-dominated field features a larger domain-averaged \mathcal{L} as compared to a field dominated by *Sugar* and *Gravels*.

Similarly, the relationship between I_{org} , \mathcal{L} and r_e might seem unexpected: Based on adiabatic parcel lifting, we would expect \mathcal{L} and r_e to be positively correlated, while Fig. 3 suggests a negative correlation. In fact, \mathcal{L} and r_e are positively correlated in our dataset, while projecting their variability on organization ($I_{org}|f_c$) suggests a negative correlation: as degree of clustering increases, \mathcal{L} increases but r_e decreases (Fig. S6). Satellite snapshots of r_e (Fig. S7) reveal that *Flowers* have substantially smaller r_e in their veils compared to their core updrafts. In contrast, *Gravels* exhibit a more homogeneous r_e with relatively larger values (compared to *Flowers*) associated with strong updrafts at the edge of their cold pool fronts. These observations suggest that for *Flowers*, the average \mathcal{L} is primarily influenced by their cores, while the average r_e is influenced by their veils. This is consistent with the fact that \mathcal{L} is proportional to r_e^6 , resulting in a more pronounced contrast between the core and veil in \mathcal{L} compared to r_e . As a result, the average \mathcal{L} of *Flowers* is larger compared to that of *Gravels*, while their average r_e is smaller in comparison to *Gravels*.

It is interesting to contrast the small droplets in relatively thick anvils described here to the very large droplet sizes and optically thin veil clouds that have been reported in the context of the stratocumulus-to-cumulus transition (Wood et al., 2018). While O, Wood, Tseng, et al. (2018) report an increase in the corresponding ultra-clean conditions with boundary layer height, this relationship is unlikely to extend to deep trade cumulus *Flowers*, which can be considered shallow mesoscale convective systems with complex outflow dynamics (Dauhut et al., 2023). On the microphysical process level, ultra clean conditions have been associated with strong precipitation scavenging (O, Wood, & Bretherton, 2018), while Radtke, Vogel, Ament, and Naumann (2023) discuss that the conversion efficiency to precipitation decreases with increasing organization in trade cumulus.

Overall, our discussion of the relationship between liquid-water path and effective radius to organization and the resulting effects on optical depth highlight that organized cloud fields cannot be conceptualized with a single, typical profile of cloudiness. Instead, the spatial variability requires considering two types of clouds as discussed for *Gravel* and *Sugar* versus *Flower* cores and anvils. This duality resonates with the effective two-dimensionality of quantitative measures for mesoscale organization (Janssens et al., 2021; Shamekh, Lamb, Huang, & Gentine, 2023).

3.3 Mean cloud geometric thickness increases with clustering

For an entraining lifting parcel, liquid-water path $\mathcal{L} \propto f_{ad}h^2$, where f_{ad} represents the degree of adiabaticity and h denotes geometric cloud thickness. To explain the observed I_{org} - \mathcal{L} relationship, we therefore investigate the relationships of I_{org} to h and f_{ad} in the *Botany* simulations. Repeating the analysis from Sects. 3.1, 3.2 for the simulation data shows qualitative agreement and thus justifies this approach (Figs. S9(a-c), S10). Note that the discrepancy in the response of r_e to cloud organization between simulations and satellite data (Fig. S9, d) is expected from the fixed cloud droplet number in the

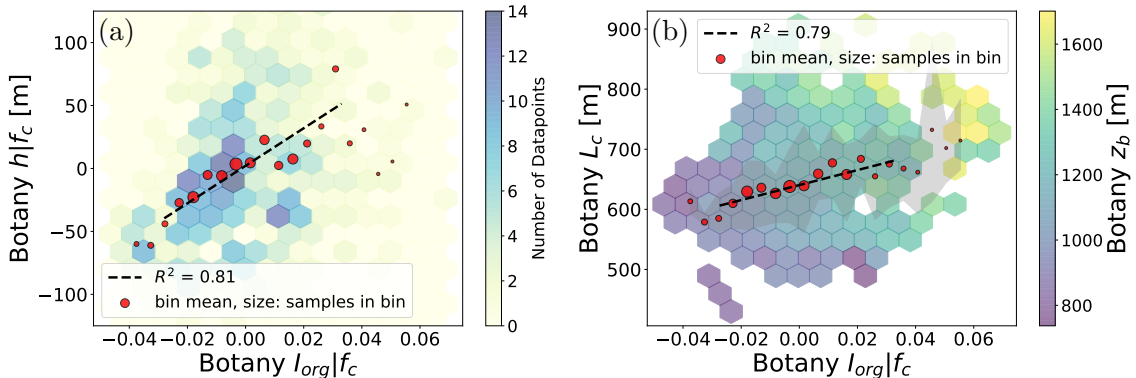


Figure 4: Dependence of domain-mean geometric thickness, average size of cloud objects, and domain-mean cloud-base height on organization. (a) The figure shows the 2D histogram of the relationship between $I_{org}|f_c$ and $h|f_c$. (b) The plot shows the relationship between $I_{org}|f_c$ and the mean-field cloud object size (L_c) with contour colors representing the values of domain-averaged cloud-base height (z_b). The gray shade indicates the inter-quartile range variability of L_c in each bin of $I_{org}|f_c$. For both plots, the mean values of $I_{org}|f_c$ in each bin are denoted by red circles, with their size proportional to the number of points in the bin. The red dots are fitted with a dashed black line. For both plots, values below the 5th and above the 95th percentile of $I_{org}|f_c$ are excluded from the fit.

simulations but does not fundamentally affect our discussion of \mathcal{L} here.

Figure 4(a) shows that the domain-averaged geometric thickness increases by more than 100 m as cloud fields become more clustered (increasing $I_{org}|f_c$). Additionally, the variability in h has a significantly larger influence on the value of \mathcal{L} than f_{ad} (Fig. S11). Thus, our LES-based results indicate that the simulated increase in \mathcal{L} due to enhanced clustering (Fig. S9, c) primarily stems from the geometric thickening of cloud fields.

Figure 4(b) further explores the relationship between horizontal and vertical cloud field properties and shows that the average size of cloud objects (L_c) increases with $I_{org}|f_c$. This positive correlation shows that cloud horizontal extent as quantified by L_c , is positively correlated to cloud vertical extent as quantified by h , consistent with the findings of Feingold et al. (2017). The figure moreover illustrates that an increase in $I_{org}|f_c$ corresponds to a rise in the domain-average cloud-base height (z_b). Note that z_b is not the lifting condensation level; instead, it represents the lowest height of a cloudy pixel within each column. This means that a higher domain-mean z_b is an indication of the presence of more anvils in the field. Overall, Fig. 4(b) demonstrates that enhanced clustering leads to a higher occurrence of larger cloud objects with elevated domain-mean z_b , indicating a higher degree of *anvilness*.

4 Conclusions & Outlook

We have explored the impact of shallow cumulus cloud field organization on cloud radiative effects, where confounding variability of f_c was removed through partial correlation analysis (Eq. 1). Based on satellite data, our analysis shows that an increased level of clustering ($I_{org}|f_c$) results in up to 20 W/m² higher SW reflection to space (Fig. 1, d,

f). We observe that, irrespective of f_c variations, more clustered cloud fields exhibit, on average, higher liquid water path (Fig. 3, a), smaller cloud droplets (Fig. 3, b), and consequently, greater optical thickness (Fig. 2). A complementing ensemble of large-eddy simulations indicates that increased clustering leads to geometrically thicker cloud fields that feature increased anvilliness (Fig. 4). Figure 5 summarizes these results. Collectively, they suggest that, eliminating the effect of f_c , the distribution of horizontal cloud sizes ultimately determines the vertical extent of clouds, subsequently influencing liquid-water path and cloud optical depth, and ultimately albedo and SWCRE.

What do our results mean in terms of the cloud feedback of trade cumulus? Myers et al. (2021) (their Supplementary Fig. 10) show that in addition to an increase in sea-surface temperature, which is not expected to trigger a notable response in trade cumulus cloudiness (Myers et al., 2021; Cesana & Del Genio, 2021), estimated inversion strength EIS is projected to moderately increase, and surface wind to slightly decrease. According to Bony et al. (2020) such an increase in EIS would favor high-cloud-fraction *Flowers* over *Gravel* and *Sugar* with lower cloud fractions. In contrast, the decreasing surface wind would favor *Sugar*. While our results highlight the tight relationship between horizontal and vertical cloud organization, whether cloud fraction and optical depth interact positively or negatively in response to drivers of organization remains an open question. To address this interplay, we need to further explore how mesoscale processes (Janssens et al., 2023; George, Stevens, Bony, Vogel, & Naumann, 2023; Vogel, Konow, Schulz, & Zuidema, 2021) modulate cloud fraction, liquid-water path, effective radii, and anvilliness.

Data Availability

The cloud masks, provided by Aqua satellites, related to NASA’s MODIS instrument, can be extracted from level-1 Atmosphere Archive & Distribution System Distributed Active Archive Center (http://dx.doi.org/10.5067/MODIS/MYD06_L2.061). The data set related to CERES instrument is made available by Synoptic TOA and surface fluxes and clouds (SYN1deg - level 3) at <https://ceres.larc.nasa.gov/data/#syn1deg-level-3>. Preprocessing of cloud masks alongside calculation of organization metrics were done using the cloud metrics Github repository (Denby & Janssens, n.d.) available at <https://github.com/cloudsci/cloudmetrics>. The Botany dataset was downloaded using the EUREC⁴A intake catalog (https://howto.eurec4a.eu/botany_dales.html). The data was analyzed utilizing Python (used libraries: Numpy (Harris et al., 2020), Pandas (Wes McKinney, 2010), Scipy (Virtanen et al., 2020), Matplotlib (Hunter, 2007), and Seaborn (Waskom, 2021)). ChatGPT (OpenAI: <https://openai.com/blog/chatgpt>) has been used for copy-editing during the preparation of the manuscript.

Acknowledgments

PA is grateful to Lousie Nuijens and Stephan de Roode for fruitful discussions. FG and PA acknowledge support from The Branco Weiss Fellowship - Society in Science, administered by ETH Zurich. FG also acknowledges a NWO Veni grant. A. PS acknowledges support from the European Union’s Horizon 2020 research and innovation program under grant agreement no. 820829 (CONSTRAIN project). TG acknowledges funding by the German Research Foundation (Deutsche Forschungsgemeinschaft, DFG; GZ QU 311/27-1)

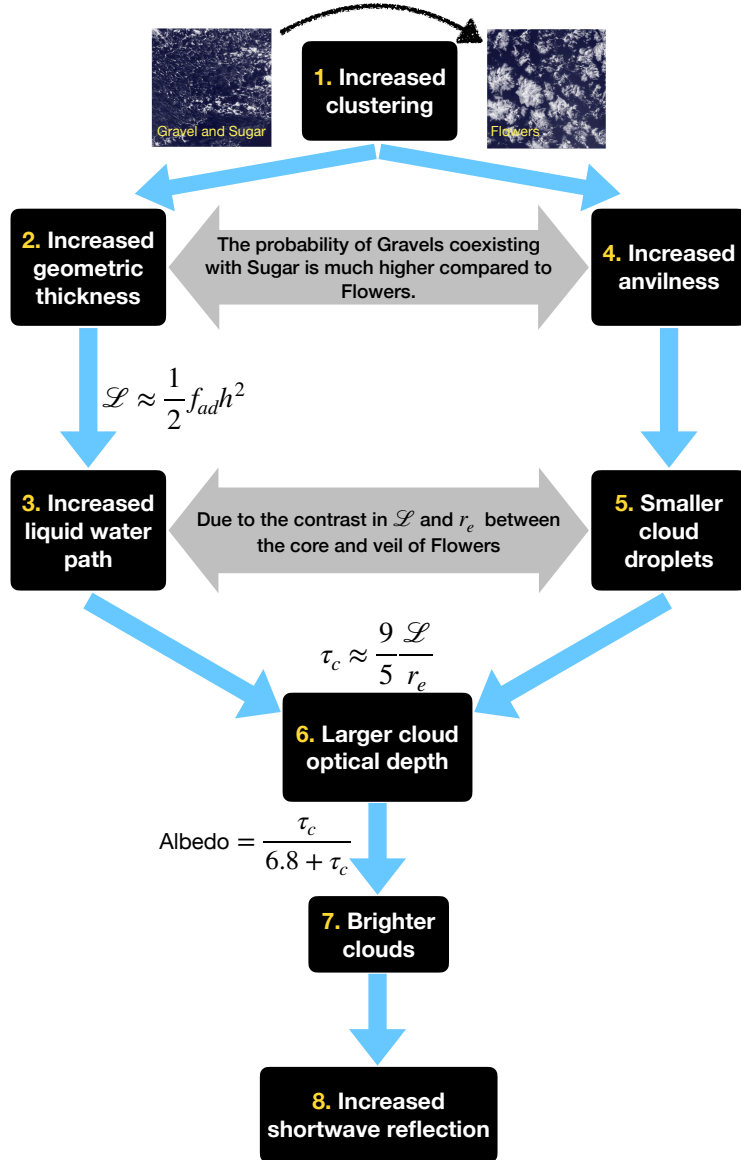


Figure 5: Summary of results. Comparing two cloud fields with identical cloud cover, the *Flower*-dominated cloud field features a larger domain-averaged geometric thickness, a higher liquid water path, more frequent anvils with smaller cloud droplets, and consequently, brighter clouds and therefore larger SW reflection in comparison to the cloud field dominated by the presence of *Sugar* and *Gravels*. In the diagram, theory-based equations are provided for arrows where the underlying theory exists. The gray arrows illustrate apparent paradoxes which are discussed in section 3.2.

for project “CDNC4ACT”. GC acknowledges startup funds from Bar-Ilan University.

References

Baba, K., Shibata, R., & Sibuya, M. (2004). Partial correlation and conditional correlation as measures of conditional independence. *Australian & New Zealand Journal of*

- Statistics*, 46(4), 657–664. doi: 10.1111/j.1467-842X.2004.00360.x
- Bony, S., & Dufresne, J.-L. (2005). Marine boundary layer clouds at the heart of tropical cloud feedback uncertainties in climate models. *Geophysical Research Letters*, 32(20). doi: 10.1029/2005GL023851
- Bony, S., Dufresne, J.-L., Le Treut, H., Morcrette, J.-J., & Senior, C. (2004). On dynamic and thermodynamic components of cloud changes. *Climate Dynamics*, 22(2), 71–86. doi: 10.1007/s00382-003-0369-6
- Bony, S., Schulz, H., Vial, J., & Stevens, B. (2020). Sugar, gravel, fish, and flowers: Dependence of mesoscale patterns of trade-wind clouds on environmental conditions. *Geophysical Research Letters*, 47(7), e2019GL085988. doi: 10.1029/2019GL085988
- Bony, S., Stevens, B., Frierson, D. M., Jakob, C., Kageyama, M., Pincus, R., ... others (2015). Clouds, circulation and climate sensitivity. *Nature Geoscience*, 8(4), 261–268. doi: 10.1038/ngeo2398
- Cesana, G. V., & Del Genio, A. D. (2021). Observational constraint on cloud feedbacks suggests moderate climate sensitivity. *Nature Climate Change*, 11(3), 213–218. doi: 10.1038/s41558-020-00970-y
- Dauhut, T., Couvreur, F., Bouniol, D., Beucher, F., Volkmer, L., Pörtge, V., ... others (2023). Flower trade-wind clouds are shallow mesoscale convective systems. *Quarterly Journal of the Royal Meteorological Society*, 149(750), 325–347. doi: 10.1002/qj.4409
- Denby, L. (2020). Discovering the importance of mesoscale cloud organization through unsupervised classification. *Geophysical Research Letters*, 47(1), e2019GL085190. doi: 10.1029/2019GL085190
- Denby, L. (2023). *Charting the realms of mesoscale cloud organisation using unsupervised learning*. doi: <https://doi.org/10.48550/arXiv.2309.08567>
- Denby, L., & Janssens, M. (n.d.). *cloudmetrics*.
- Eytan, E., Koren, I., Altaratz, O., Kostinski, A. B., & Ronen, A. (2020). Longwave radiative effect of the cloud twilight zone. *Nature Geoscience*, 13(10), 669–673. doi: 10.1038/s41561-020-0636-8
- Eytan, E., Koren, I., Altaratz, O., Pinsky, M., & Khain, A. (2021). Revisiting adiabatic fraction estimations in cumulus clouds: high-resolution simulations with a passive tracer. *Atmospheric Chemistry and Physics*, 21(21), 16203–16217. doi: 10.5194/acp-21-16203-2021
- Feingold, G., Balsells, J., Glassmeier, F., Yamaguchi, T., Kazil, J., & McComiskey, A. (2017). Analysis of albedo versus cloud fraction relationships in liquid water clouds using heuristic models and large eddy simulation. *Journal of Geophysical Research: Atmospheres*, 122(13), 7086–7102. doi: 10.1002/2017JD026467
- George, G., Stevens, B., Bony, S., Vogel, R., & Naumann, A. K. (2023). Widespread shallow mesoscale circulations observed in the trades. *Nature Geoscience*, 1–6. doi: 10.1038/s41561-023-01215-1
- Han, Q., Rossow, W. B., & Lacis, A. A. (1994). Near-global survey of effective droplet radii in liquid water clouds using isccp data. *Journal of Climate*, 7(4), 465–497. doi: 10.1175/1520-0442(1994)007<0465:NGSOED>2.0.CO;2
- Harris, C. R., Millman, K. J., van der Walt, S. J., Gommers, R., Virtanen, P., Cournapeau, D., ... Oliphant, T. E. (2020, September). Array programming with NumPy. *Nature*, 585(7825), 357–362. Retrieved from <https://doi.org/10.1038/s41586-020-2649-2> doi: 10.1038/s41586-020-2649-2
- Hersbach, H., Bell, B., Berrisford, P., Hirahara, S., Horányi, A., Muñoz-Sabater, J., ... others (2020). The ERA5 global reanalysis. *Quarterly Journal of the Royal Meteorological Society*, 146(10), 1999–2049. doi: 10.1002/qj.3990

- rological Society*, 146(730), 1999–2049. doi: 10.1002/qj.3803
- Hunter, J. D. (2007). Matplotlib: A 2D graphics environment. *Computing in Science & Engineering*, 9(3), 90–95. doi: 10.1109/MCSE.2007.55
- Janssens, M., de Arellano, J. V.-G., van Heerwaarden, C. C., de Roode, S. R., Siebesma, A. P., & Glassmeier, F. (2023). Nonprecipitating shallow cumulus convection is intrinsically unstable to length scale growth. *Journal of the Atmospheric Sciences*, 80(3), 849–870. doi: 10.1175/JAS-D-22-0111.1
- Janssens, M., Vilà-Guerau de Arellano, J., Scheffer, M., Antonissen, C., Siebesma, A. P., & Glassmeier, F. (2021). Cloud patterns in the trades have four interpretable dimensions. *Geophysical Research Letters*, 48(5), e2020GL091001. doi: 10.1029/2020GL091001
- Jansson, F., Janssens, M., Grönqvist, J. H., Siebesma, P., Glassmeier, F., Attema, J. J., ... others (2023). Cloud botany: Shallow cumulus clouds in an ensemble of idealized large-domain large-eddy simulations of the trades. *submitted to Journal of Advances in Modeling Earth Systems, preprint: <https://www.authorea.com/doi/full/10.22541/essoar.168319841.11427814>*. doi: 10.22541/essoar.168319841.11427814/v1
- Johnson, R. H., Rickenbach, T. M., Rutledge, S. A., Ciesielski, P. E., & Schubert, W. H. (1999). Trimodal characteristics of tropical convection. *Journal of climate*, 12(8), 2397–2418. doi: 10.1175/1520-0442(1999)012<2397:TCOTC>2.0.CO;2
- Luebke, A. E., Ehrlich, A., Schäfer, M., Wolf, K., & Wendisch, M. (2022). An assessment of macrophysical and microphysical cloud properties driving radiative forcing of shallow trade-wind clouds. *Atmospheric Chemistry and Physics*, 22(4), 2727–2744. doi: 10.5194/acp-22-2727-2022
- McCoy, I. L., McCoy, D. T., Wood, R., Zuidema, P., & Bender, F. A.-M. (2022). The role of mesoscale cloud morphology in the shortwave cloud feedback. *Geophysical Research Letters*, e2022GL101042. doi: 10.1029/2022GL101042
- Medeiros, B., & Nuijens, L. (2016). Clouds at Barbados are representative of clouds across the trade wind regions in observations and climate models. *Proceedings of the National Academy of Sciences*, 113(22), E3062–E3070. doi: 10.1073/pnas.1521494113
- Myers, T. A., Scott, R. C., Zelinka, M. D., Klein, S. A., Norris, J. R., & Caldwell, P. M. (2021). Observational constraints on low cloud feedback reduce uncertainty of climate sensitivity. *Nature Climate Change*, 11(6), 501–507. doi: 10.1038/s41558-021-01039-0
- Nuijens, L., & Siebesma, A. P. (2019). Boundary layer clouds and convection over subtropical oceans in our current and in a warmer climate. *Current Climate Change Reports*, 5(2), 80–94. doi: 10.1007/s40641-019-00126-x
- O, K.-T., Wood, R., & Bretherton, C. S. (2018). Ultraclean layers and optically thin clouds in the stratocumulus-to-cumulus transition. Part II: Depletion of cloud droplets and cloud condensation nuclei through collision–coalescence. *Journal of the Atmospheric Sciences*, 75(5), 1653–1673. doi: 10.1175/JAS-D-17-0218.1
- O, K.-T., Wood, R., Tseng, H., et al. (2018). Deeper, precipitating PBLs associated with optically thin veil clouds in the Sc-Cu transition. *Geophysical Research Letters*, 45(10), 5177–5184. doi: 10.1029/2018GL077084
- Painemal, D., & Zuidema, P. (2011). Assessment of MODIS cloud effective radius and optical thickness retrievals over the southeast pacific with VOCALS-REX in situ measurements. *Journal of Geophysical Research: Atmospheres*, 116(D24). doi: 10.1029/2011JD016155
- Radtke, J., Vogel, R., Ament, F., & Naumann, A. K. (2023). Spa-

- tial organisation affects the pathway to precipitation in simulated trade-wind convection. *Submitted to Geophysical Research Letters, preprint: <https://www.authorea.com/doi/full/10.22541/essoar.167979635.58663858>*. doi: 10.22541/essoar.167979635.58663858/v2
- Schmeissner, T., Shaw, R., Ditas, J., Stratmann, F., Wendisch, M., & Siebert, H. (2015). Turbulent mixing in shallow trade wind cumuli: Dependence on cloud life cycle. *Journal of the Atmospheric Sciences*, *72*(4), 1447–1465. doi: 10.1175/JAS-D-14-0230.1
- Schneider, T., Teixeira, J., Bretherton, C. S., Briant, F., Pressel, K. G., Schär, C., & Siebesma, A. P. (2017). Climate goals and computing the future of clouds. *Nature Climate Change*, *7*(1), 3–5. doi: 10.1038/nclimate3190
- Schulz, H., Eastman, R., & Stevens, B. (2021). Characterization and evolution of organized shallow convection in the trades. *Journal of Geophysical Research: Atmospheres*. doi: 10.1029/2021JD034575
- Seethala, C., & Horváth, Á. (2010). Global assessment of AMSR-E and MODIS cloud liquid water path retrievals in warm oceanic clouds. *Journal of Geophysical Research: Atmospheres*, *115*(D13). doi: 10.1029/2009JD012662
- Shamekh, S., Lamb, K. D., Huang, Y., & Gentine, P. (2023). Implicit learning of convective organization explains precipitation stochasticity. *Proceedings of the National Academy of Sciences*, *120*(20), e2216158120. doi: 10.1073/pnas.2216158120
- Sherwood, S. C., Webb, M. J., Annan, J. D., Armour, K. C., Forster, P. M., Hargreaves, J. C., . . . others (2020). An assessment of Earth’s climate sensitivity using multiple lines of evidence. *Reviews of Geophysics*, *58*(4), e2019RG000678. doi: 10.1029/2019RG000678
- Singer, C. E., Lopez-Gomez, I., Zhang, X., & Schneider, T. (2021). Top-of-atmosphere albedo bias from neglecting three-dimensional cloud radiative effects. *Journal of the Atmospheric Sciences*, *78*(12), 4053–4069. doi: 10.1175/JAS-D-21-0032.1
- Stevens, B., Bony, S., Brogniez, H., Hentgen, L., Hohenegger, C., Kiemle, C., . . . others (2020). Sugar, gravel, fish and flowers: Mesoscale cloud patterns in the trade winds. *Quarterly Journal of the Royal Meteorological Society*, *146*(726), 141–152. doi: 10.1002/qj.3662
- Tobin, I., Bony, S., & Roca, R. (2012). Observational evidence for relationships between the degree of aggregation of deep convection, water vapor, surface fluxes, and radiation. *Journal of Climate*, *25*(20), 6885–6904. doi: 10.1175/JCLI-D-11-00258.1
- Tompkins, A. M., & Semie, A. G. (2017). Organization of tropical convection in low vertical wind shears: Role of updraft entrainment. *Journal of Advances in Modeling Earth Systems*, *9*(2), 1046–1068. doi: 10.1002/2016MS000802
- Virtanen, P., Gommers, R., Oliphant, T. E., Haberland, M., Reddy, T., Cournapeau, D., . . . SciPy 1.0 Contributors (2020). SciPy 1.0: Fundamental Algorithms for Scientific Computing in Python. *Nature Methods*, *17*, 261–272. doi: 10.1038/s41592-019-0686-2
- Vogel, R., Albright, A. L., Vial, J., George, G., Stevens, B., & Bony, S. (2022). Strong cloud–circulation coupling explains weak trade cumulus feedback. *Nature*, 1–5. doi: 10.1038/s41586-022-05364-y
- Vogel, R., Konow, H., Schulz, H., & Zuidema, P. (2021). A climatology of trade-wind cumulus cold pools and their link to mesoscale cloud organization. *Atmospheric Chemistry and Physics*, *21*(21), 16609–16630. doi: 10.5194/acp-21-16609-2021
- Waskom, M. L. (2021). seaborn: statistical data visualization. *Journal of Open Source Software*, *6*(60), 3021. Retrieved from <https://doi.org/10.21105/joss.03021>

doi: 10.21105/joss.03021

- Weger, R., Lee, J., Zhu, T., & Welch, R. (1992). Clustering, randomness and regularity in cloud fields: 1. Theoretical considerations. *Journal of Geophysical Research: Atmospheres*, 97(D18), 20519–20536. doi: 10.1029/92JD02038
- Wes McKinney. (2010). Data Structures for Statistical Computing in Python. In Stéfan van der Walt & Jarrod Millman (Eds.), *Proceedings of the 9th Python in Science Conference* (p. 56 - 61). doi: 10.25080/Majora-92bf1922-00a
- Wood, R., O, K.-T., Bretherton, C. S., Mohrmann, J., Albrecht, B. A., Zuidema, P., ... others (2018). Ultraclean layers and optically thin clouds in the stratocumulus-to-cumulus transition. Part I: Observations. *Journal of the Atmospheric Sciences*, 75(5), 1631–1652. doi: 10.1175/JAS-D-17-0213.1
- Zhang, Z., & Platnick, S. (2011). An assessment of differences between cloud effective particle radius retrievals for marine water clouds from three MODIS spectral bands. *Journal of Geophysical Research: Atmospheres*, 116(D20). doi: 10.1029/2011JD016216

**Supplementary Information for “Shallow Cumulus Cloud
Fields Are Optically Thicker When They Are More
Clustered”**

This file includes some additional figures for supporting the main text of our paper (First part). Additionally, the detailed calculation of adiabaticity is presented (Second part).

Supplementary Figures

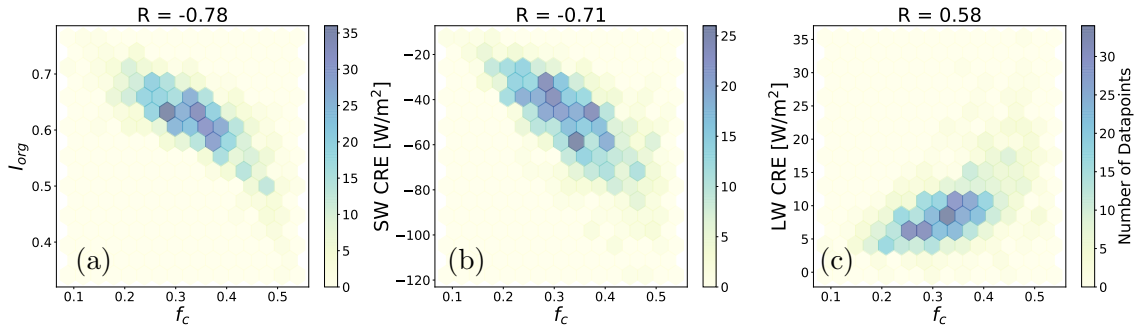


Figure S1: The 2D histograms of the relationships between f_c and (a) I_{org} , (b) SWCRE, and (c) LWCRE with the reported Pearson's correlation (R).

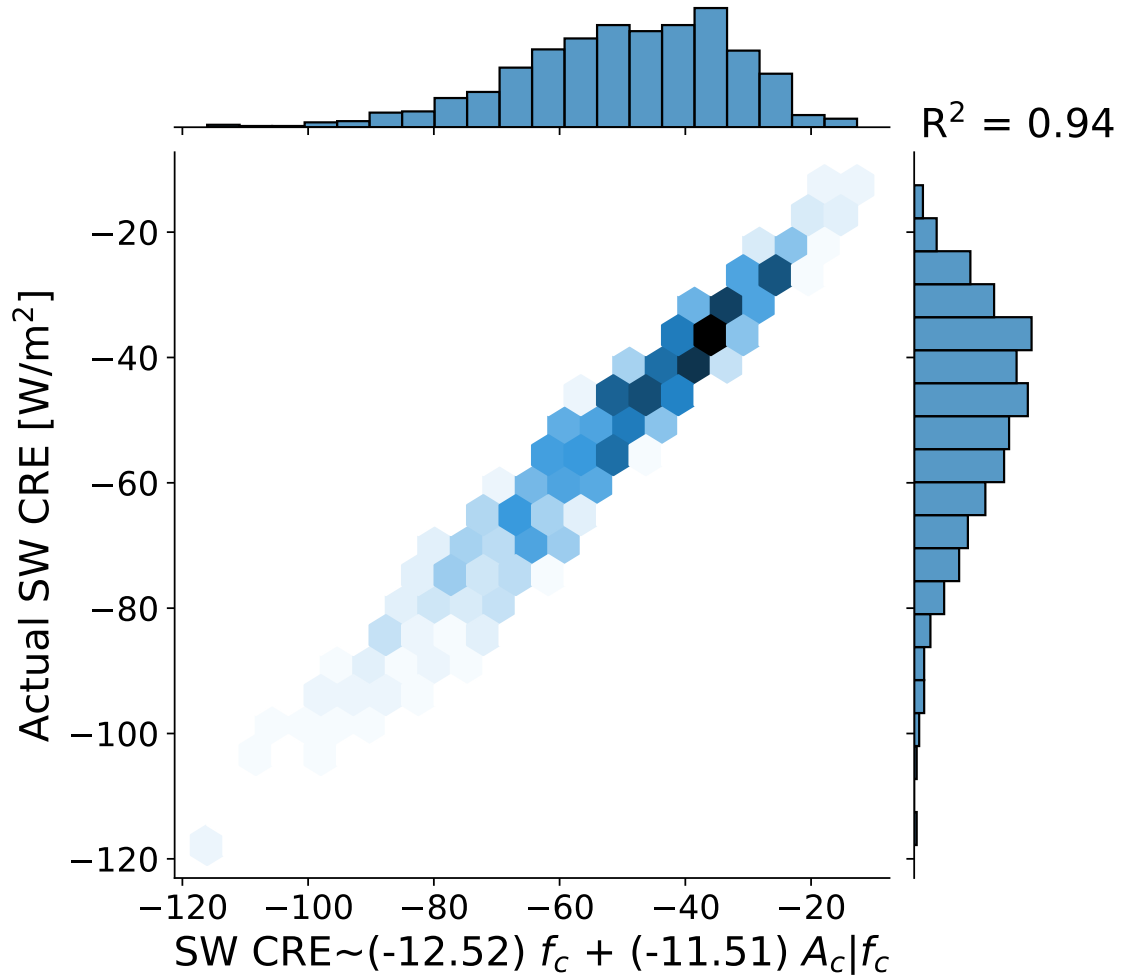


Figure S2: The result of the bi-linear regression analysis in which the target value is SWCRE and the regressors are f_c and $A_c | f_c$ (A_c : cloud albedo observed by CERES). The reported coefficients are for the standardized f_c and $A_c | f_c$. This plots ensures that the derived f_c from MODIS cloud masks in addition to the observed albedo by CERES can significantly capture the variability in SWCRE.

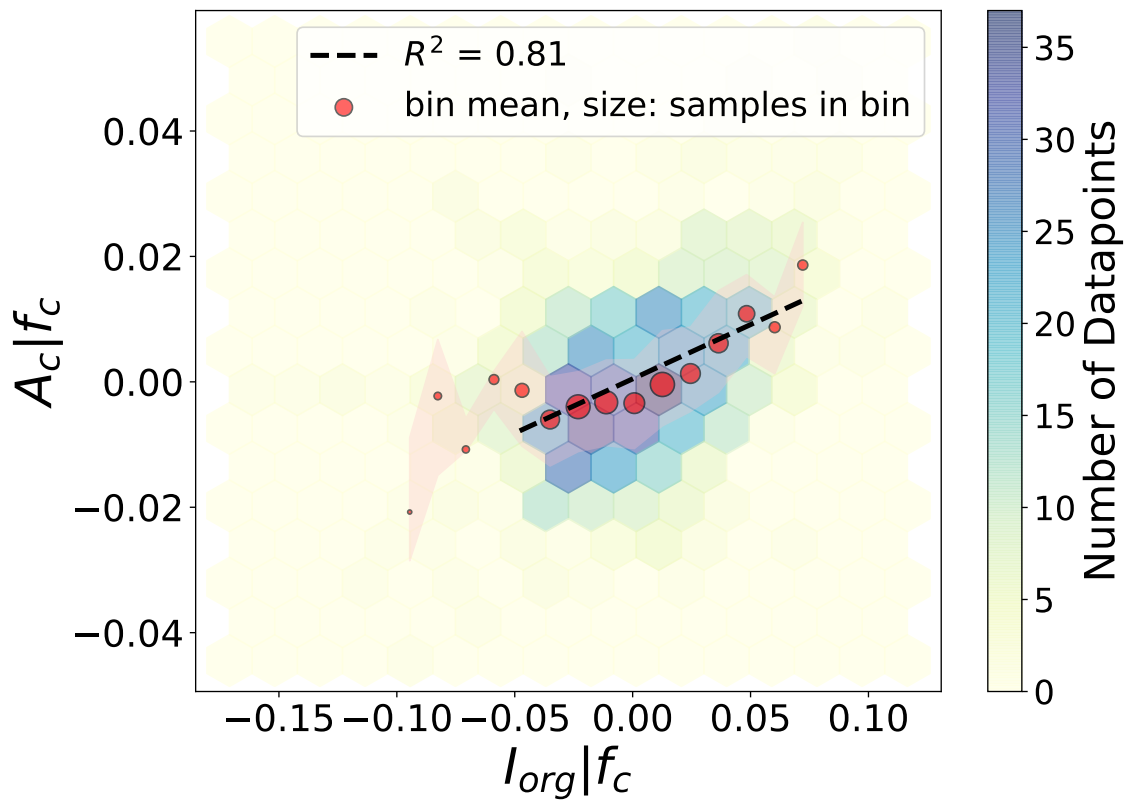


Figure S3: The relationship between I_{org} and cloud albedo (A_c), having the effect of f_c eliminated.

Calculation of the degree of adiabaticity

The degree of adiabaticity is computed using the following equation:

$$f_{ad} = \frac{\int_{z_b}^{z_t} \rho(z) q_l(z) dz}{\int_{z_b}^{z_t} \rho(z) \Gamma_{ad}(z) z dz} \quad (2)$$

where, z represents the height, $\rho(z)$, $q_l(z)$, and $\Gamma_{ad}(z)$ denotes density, liquid water specific humidity, and the moist adiabatic lapse rate of q_l at each model height. To ensure a more precise estimation, f_{ad} is computed only for columns where the associated z_b is in proximity to the lifting condensation level (<850 m) and the cloud thickness exceeds 150 m.

The calculation of Γ_{ad} is determined by the following equation (Schmeissner et al., 2015; Eytan, Koren, Altaratz, Pinsky, & Khain, 2021):

$$\Gamma_{ad} = \frac{c_p}{L_v} \left(\Gamma_m + \frac{g}{c_p} \right) \quad (3)$$

Here, c_p represents the specific heat constant, g denotes the acceleration due to gravity, L_v stands for the latent heat of vaporization. The moist adiabatic lapse rate for temperature, Γ_m , is computed as:

$$\Gamma_m = \frac{g}{c_p} \left(\frac{1 + \frac{L_v}{R_d T} q_s}{1 + \frac{\beta L_v}{c_p} q_s} \right) \quad (4)$$

In the above equation, R_d corresponds to the gas constant for dry air, T represents temperature, β is the constant in the Clausius-Clapeyron equation ($e_s = A \exp(\beta(T - T_0))$), and q_s denotes the saturation specific humidity, which can be approximated as $\approx 0.622 \frac{e_s}{P}$ where P represents pressure.

For simplicity, we calculate Γ_{ad} for the middle of the cloud layer (at $z' = \frac{z_b + z_t}{2}$) and assume that it linearly changes with height through the cloud layer. This assumption leads to the equation below:

$$f_{ad} = \frac{\int_{z_b}^{z_t} \rho(z) q_l(z) dz}{\Gamma_{ad}(z') \int_{z_b}^{z_t} \rho(z) z dz} \quad (5)$$

where, a f_{ad} value of 1 in each column indicates a fully adiabatic cloud, while values smaller than 1 and larger than 0 indicate non-adiabatic clouds. In the final step, after obtaining f_{ad} for each column, we proceed to calculate the domain-mean f_{ad} for the entire cloud field.

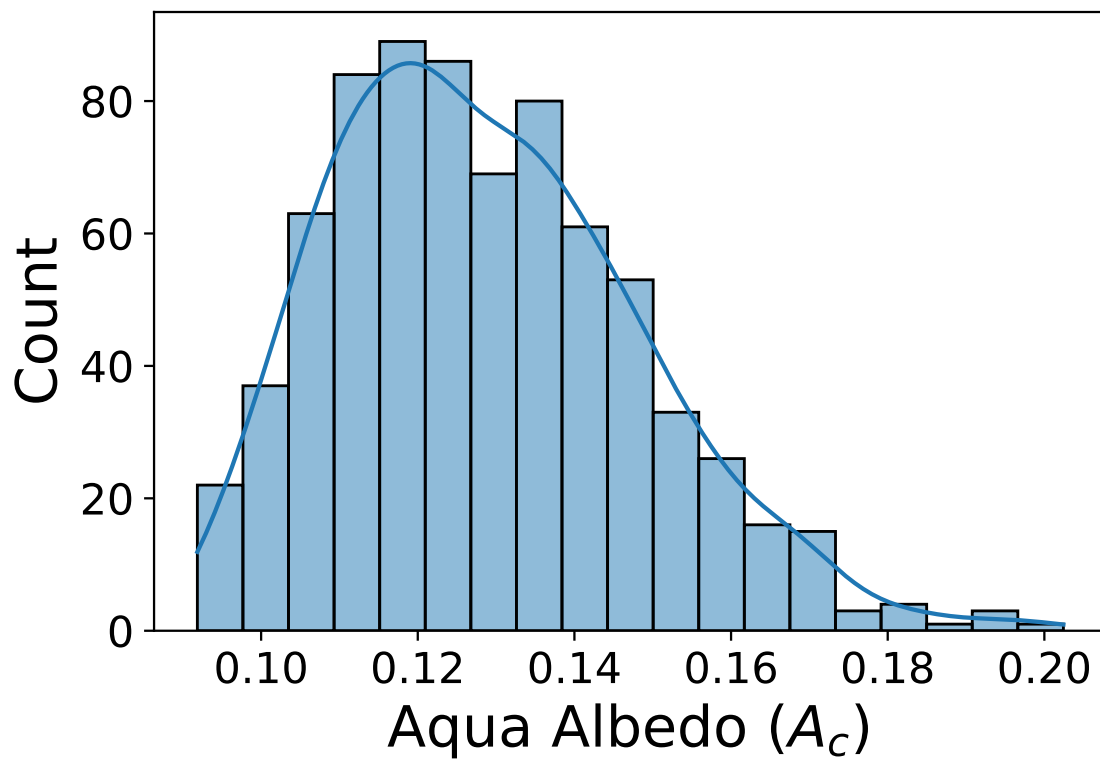


Figure S4: The histogram plot of cloud scene albedo (A_c) in the Aqua satellite dataset. This plot shows that the range of variability in cloud field albedo is about 0.1.

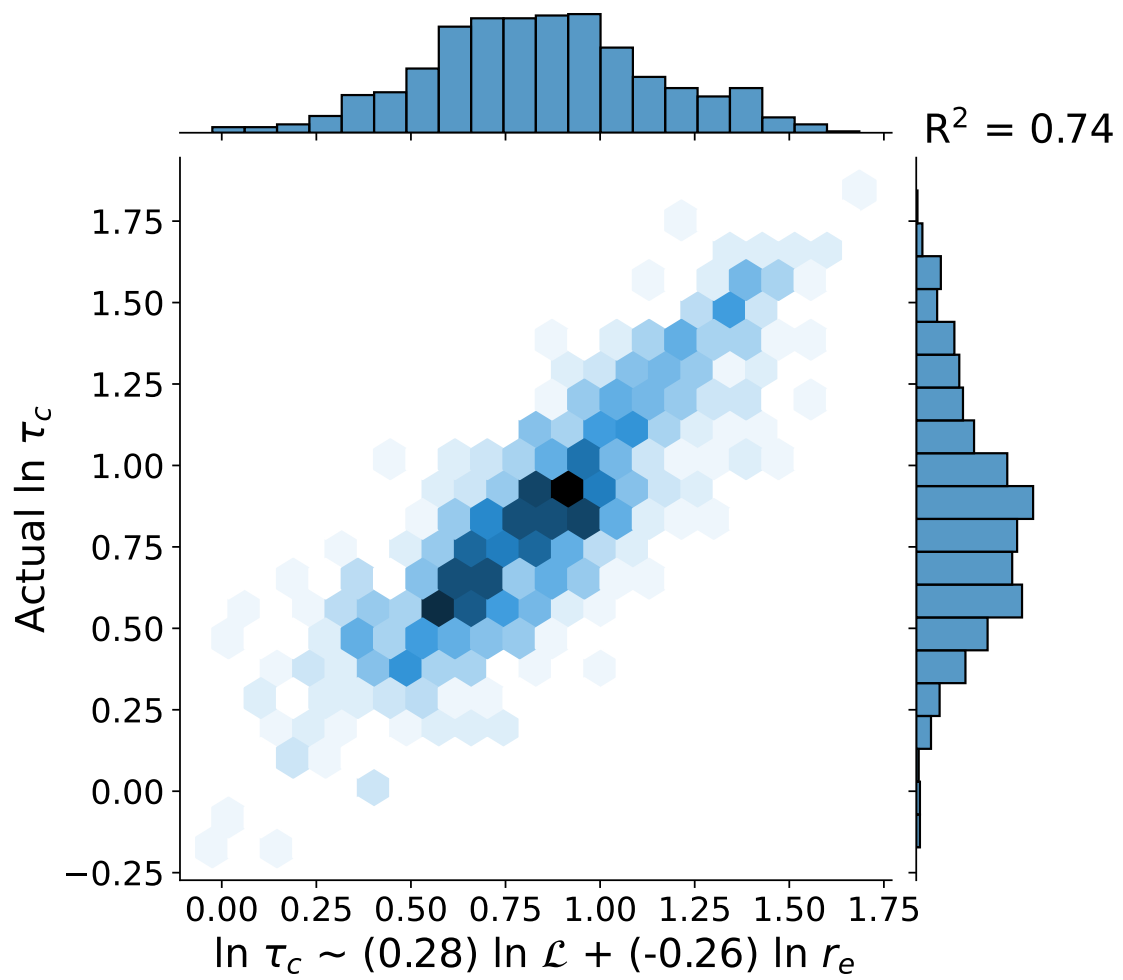


Figure S5: The result of the bi-linear regression analysis in which the target value is $\ln \tau_c$ and the regressors are $\ln \mathcal{L}$ and $\ln r_e$. The reported coefficients are for the standardized $\ln \mathcal{L}$ and $\ln r_e$. This plots ensures that $\ln \mathcal{L}$ and $\ln r_e$ can significantly capture the variability in $\ln \tau_c$, in line with theory.

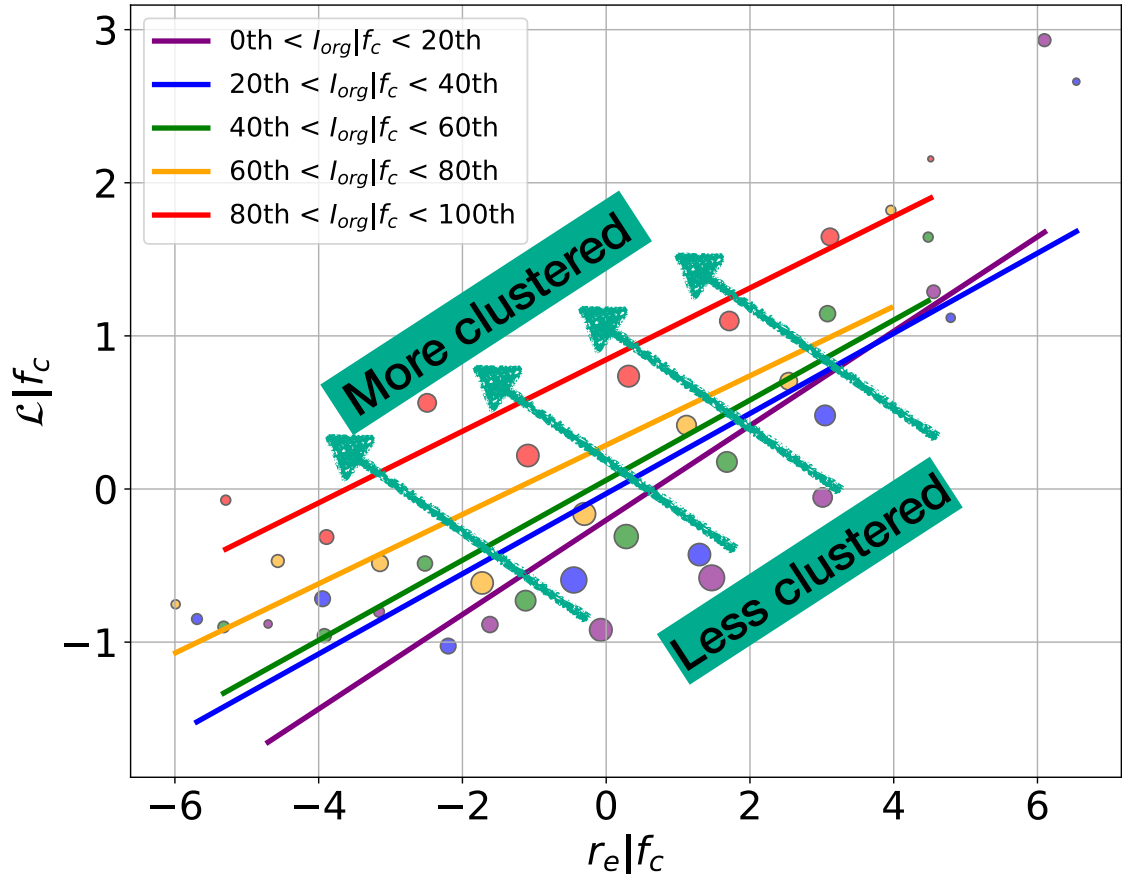


Figure S6: This figure highlights the positive correlation between \mathcal{L} and r_e . However, when we examine the \mathcal{L} - r_e relationship in relation to clustering, a clear pattern emerges: as clustering increases (more *Flowers*), \mathcal{L} increases while r_e decreases. Each distinct color in the figure represents a specific class of organization. For instance, the purple color represents cloud fields where the value of $I_{org}|f_c$ falls within the range of the 0th to 10th percentile of $I_{org}|f_c$.

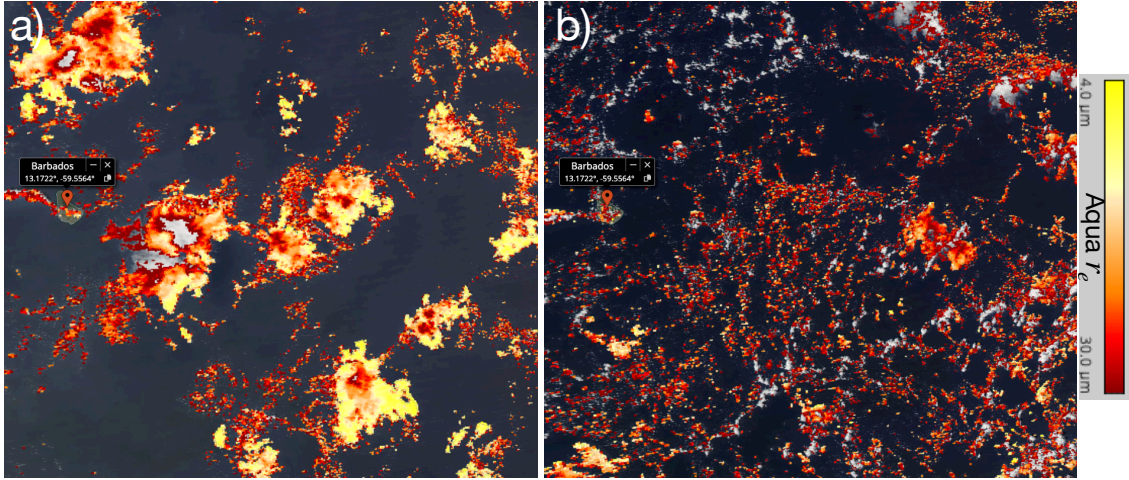


Figure S7: A Flowers (a) and a Gravel cloud field snapshots (from NASA Worldview) taken by Aqua satellites on 02/Feb/2020 and 17/Jan/2020, respectively. The cloud fields are colored by the value of r_e which goes from 4 (yellow) to 30 (red) μm .

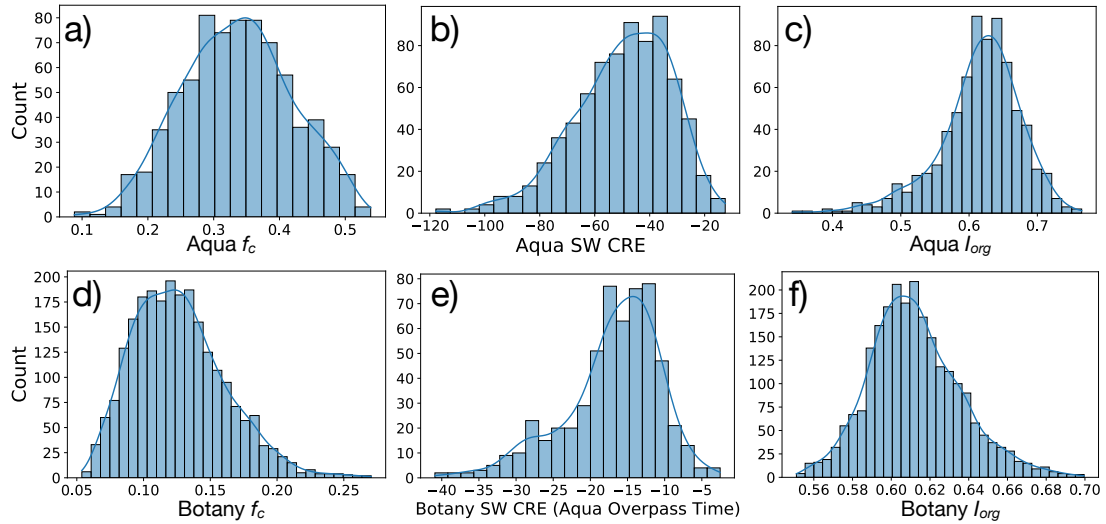


Figure S8: Histograms of f_c , SWCRE and I_{org} for Aqua (a,b,c) and Botany (d,e,f) datasets, respectively. The values of SWCRE are in W/m^2 . Note that the histograms of f_c and I_{org} are for the whole Botany dataset, while the Botany's SWCRE is only for hours 37-43 (day-time values).

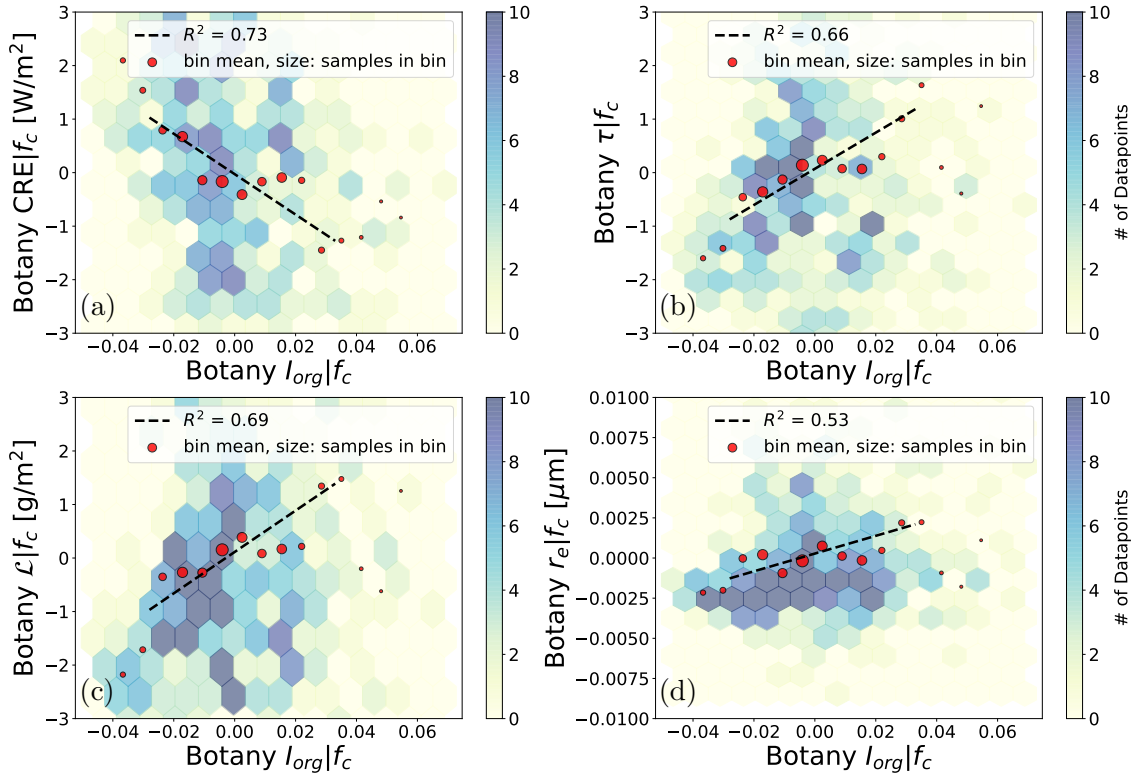


Figure S9: All results derived from the hourly analysis of the Cloud Botany dataset during the second day between the 37th and 43rd hours. Values below the 5th and above the 95th percentile of $I_{org}|f_c$ are excluded from the fitting.

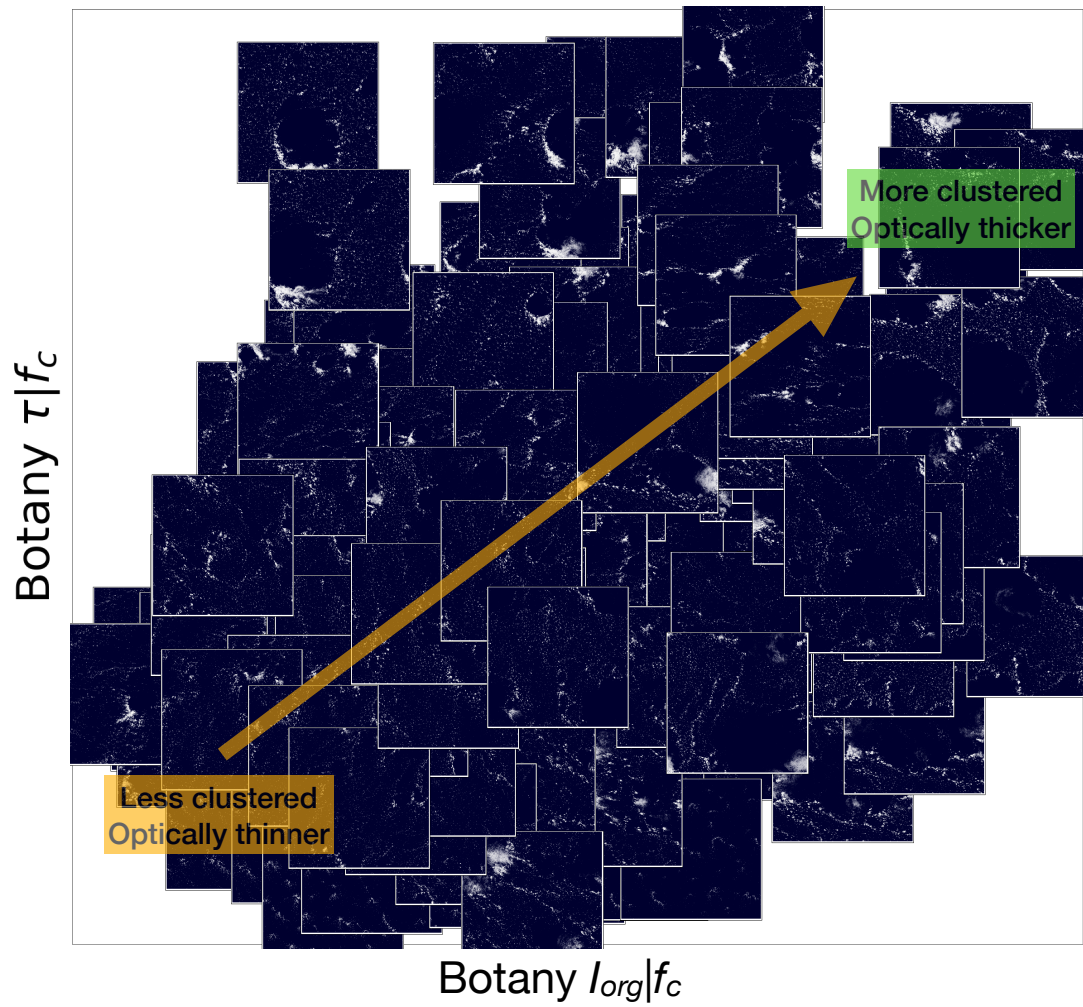


Figure S10: Similar to Fig. 2(a) but for the Botany dataset during hours 37-43.

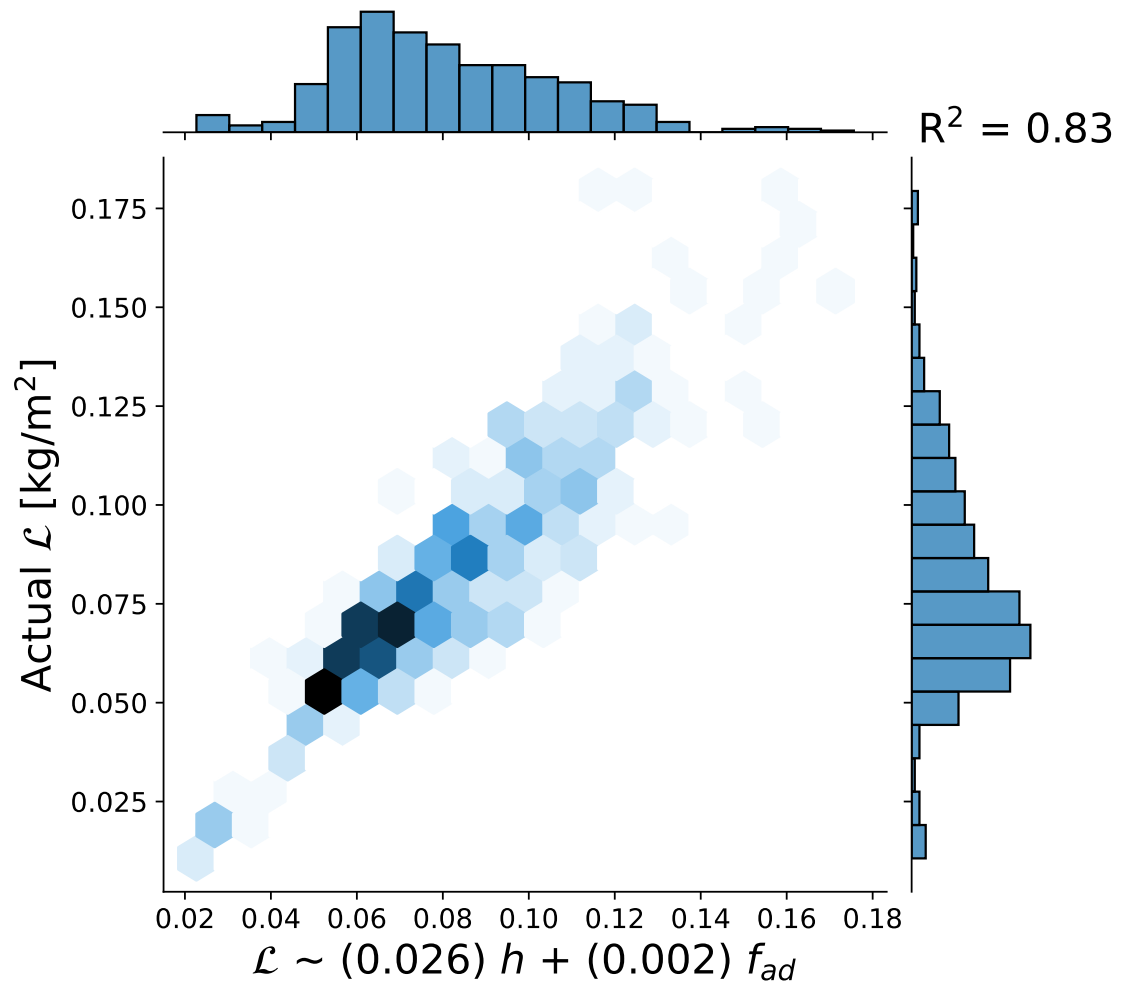


Figure S11: The result of the bi-linear regression analysis in which the target value is the in-cloud \mathcal{L} and the regressors are h and f_{ad} . The reported coefficients are for the standardized h and f_{ad} .